
Proximal-IMH: Proximal Posterior Proposals for Independent Metropolis–Hastings with Approximate Operators

Youguang Chen¹ George Biros¹

Abstract

We are considering the problem of sampling from a posterior distribution related to Bayesian inverse problems arising in science, engineering, and imaging. Our method belongs to the family of independence Metropolis–Hastings (IMH) sampling algorithms. These are quite common in Bayesian inference. Relying on the existence of an approximate posterior distribution that is cheaper to sample from but can have significant bias, we introduce Proximal-IMH, a scheme that removes this bias: it corrects samples from the approximate posterior solving an auxiliary optimization problem, yielding a local adjustment that trades off adherence to the exact model against stability around the approximate reference point. For idealized settings, we prove that the proximal correction tightens the match between approximate and exact posteriors, and thereby improves acceptance rates and mixing. The new method works with both linear and nonlinear input-output operators and is especially suitable for inverse problems where exact posterior sampling is too expensive. We perform several numerical experiments that include multimodal and data-driven priors and nonlinear input-output operators. The results show that Proximal-IMH reliably outperforms existing IMH variants.

$q(e)$. Here, \mathbf{O} is a linear *observation operator*, $\mathbf{F}(x)$ is a (possibly nonlinear) *forward operator*, and $\mathbf{A} = \mathbf{O}\mathbf{F}$ is the associated *input–output operator*. The operator \mathbf{F} typically corresponds to the solution map of a differential or integral equation driven by the parameter x , and $u = \mathbf{F}(x)$ is a latent variable representing this solution. As an example from acoustics, x may describe an unknown scatterer, u is the resulting acoustic field—defined everywhere; and y consists of measurements collected at sensor locations. The Bayesian posterior distribution is given by $\pi(x | y) \propto q(y - \mathbf{O}\mathbf{F}(x)) p(x)$. Our goal is to design fast and scalable algorithms for efficiently generating samples from $\pi(x | y)$.

Inverse problems of the form Equation (1) arise in a wide range of applications, including tomography (Kaipio et al., 2000; Saratoon et al., 2013; Arridge & Schotland, 2009), medical imaging (Liang et al., 2020; Epstein, 2007), geophysics (Tarantola, 2005), and many others (Kaipio & Somersalo, 2006; Vogel, 2002; Ghattas & Willcox, 2021). In many such problems, evaluating the forward operator \mathbf{F} is computationally expensive, but a cheaper approximation $\tilde{\mathbf{F}}$ is available such that $\tilde{\mathbf{F}}(x) \approx \mathbf{F}(x)$. Defining $\tilde{\mathbf{A}} = \mathbf{O}\tilde{\mathbf{F}}$, this naturally leads to the *approximate posterior* $\pi_a(x | y) \propto q(y - \tilde{\mathbf{A}}(x)) p(x)$. Examples of $\tilde{\mathbf{F}}$ include preconditioners, truncated iterative solvers, coarse-grid discretizations, and learned surrogate or neural operators (Cohen et al., 2014; Van der Vorst, 2003; Henson & Yang, 2002; Herrmann et al., 2024).

A broad class of methods has been developed for sampling from $\pi(x | y)$, including Markov chain Monte Carlo (MCMC) methods such as Langevin methods (Girolami & Calderhead, 2011), NUTS (Hoffman et al., 2014), and Metropolis adjusted Langevin algorithm (MALA) (Roberts & Tweedie, 1996), generative models (Song et al., 2021), normalizing flows (Papamakarios et al., 2021), low-rank approximations (Spantini et al., 2015), and many others (Biegler et al., 2010).

Several methods seek to exploit the availability of an approximate forward operator $\tilde{\mathbf{F}}$ to reduce computational cost. Among them, two approaches are particularly relevant to this work: Latent-IMH and multifidelity sampling. Multifidelity sampling methods, including delay-acceptance and

1. Introduction

We consider linear and nonlinear inverse problems of the form

$$y = \mathbf{O}\mathbf{F}(x) + e = \mathbf{A}(x) + e, \quad (1)$$

where $x \in \mathbb{R}^{d_x}$ denotes the unknown parameter vector with prior $p(x)$, $y \in \mathbb{R}^{d_y}$ is the noise-corrupted observation, and e is observational noise with known distribution

¹Oden Institute for Computational Engineering and Sciences, University of Texas at Austin, Austin, USA. Correspondence to: Youguang Chen <youguang@utexas.edu>.

two-stage algorithms (Peherstorfer et al., 2018), use $\tilde{\mathbf{F}}$ to screen or precondition proposals from a local MCMC kernel. While this reduces the number of expensive forward evaluations, the resulting schemes remain inherently local, with mixing governed by the underlying proposal. Latent-IMH (Chen & Biros, 2026) constructs a global independence proposal that preserves the exact likelihood while modifying the prior via an approximate operator, enabling efficient global moves. However, it requires transforming the forward operator into a square, invertible form and constructing an approximate distribution in a high-dimensional latent space, which can lead to ill-conditioning. We review Latent-IMH in Section 2 and include it as a baseline in our numerical experiments.

In this paper, we introduce an IMH sampler that exploits $\tilde{\mathbf{F}}$ and addresses key limitations of Latent-IMH. Our contributions are summarized below. **1** We introduce the Proximal-IMH sampling method for inverse problems of the form Equation (1) that exploits a computationally cheap approximate operator $\tilde{\mathbf{F}}$, and applies to both linear (Section 3.1) and nonlinear (Section 3.4) forward models. **2** For linear forward models, we provide a theoretical analysis showing that Proximal-IMH achieves smaller expected KL divergence (Section 3.2) and faster mixing times (Section 3.3) than existing IMH proposals under suitable regularity assumptions. **3** We demonstrate the effectiveness of Proximal-IMH on a range of linear and nonlinear inverse problems, including bimodal targets, imaging problems with learned priors, and nonlinear acoustic scattering (Section 4). Across all tests, Proximal-IMH consistently outperforms other IMH schemes in terms of acceptance rates, convergence speed, and sampling accuracy.

2. Background

We begin by defining the exact posterior and two approximate posteriors.

$$\text{Exact: } \pi(x | y) \propto q(y - \mathbf{A}x) p(x), \quad (2a)$$

$$\text{Approx: } \pi_a(x | y) \propto q(y - \tilde{\mathbf{A}}x) p(x), \quad (2b)$$

$$\text{Latent: } \pi_l(x | y) \propto q(y - \mathbf{A}x) p(\tilde{\mathbf{F}}^{-1}\mathbf{F}x), \quad (2c)$$

where the formulation for Latent posterior assumes that \mathbf{F} and $\tilde{\mathbf{F}}$ are linear and invertible. The approximate distributions π_a and π_l can be used as proposal densities $g(x | y)$ in the independence Metropolis–Hastings (IMH) algorithm (Algorithm 1).

A key advantage of IMH over local MCMC methods is that proposals are independent of the current state. Consequently, the computationally expensive computations involving the forward operator \mathbf{F} —including those required for proposal construction and the corresponding terms in the acceptance ratio—can be precomputed in advance and evaluated in

Algorithm 1 Independence Metropolis-Hastings (IMH)

In: y , number of MH steps k , proposal $g(x | y)$

Out: Samples $\{x_i\}_{i=1}^{k+1}$ from $\pi(x | y)$

1: $x_1 \sim g(x | y)$

2: **for** $t = 1$ to k **do**

3: $x' \sim g(x | y)$

4: $a(x', x_t) = \min\left\{1, \frac{\pi(x'|y)g(x_t|y)}{\pi(x_t|y)g(x'|y)}\right\}$

5: Accept x' with probability $a(x', x_t)$

6: **otherwise** set $x_{t+1} \leftarrow x_t$

7: **end for**

an embarrassingly parallel fashion. In practice, this can lead to substantial wall-clock savings for large-scale inverse problems. The efficiency of IMH is therefore governed by the acceptance ratio: for a fixed accuracy target, lower acceptance rates require more Metropolis–Hastings steps and hence more evaluations of the exact forward operator, increasing the overall computational cost. Using Approx posterior as the proposal is computationally attractive, but for Gaussian noise the log-acceptance ratio scales as $1/\sigma^2$, causing small operator errors in $\tilde{\mathbf{A}}$ to be strongly amplified and leading to poor acceptance rates in practice.

The Latent-IMH method (Chen & Biros, 2026) addresses this issue by preserving the exact likelihood $q(y - \mathbf{A}x)$ in the proposal distribution. This is achieved by sampling in the latent variable $u = \tilde{\mathbf{F}}x$. Specifically, samples are first drawn from an approximate latent prior $\tilde{p}(u)$ constructed offline, then conditioned on y using only the inexpensive observation operator \mathbf{O} , and finally mapped back via $x = \mathbf{F}^{-1}u$. This procedure is equivalent to using Equation (2c) as the IMH proposal. While effective, Latent-IMH requires squaring \mathbf{F} to enforce invertibility, which can introduce ill-conditioning, and relies on constructing the approximate distribution $\tilde{p}(u)$.

3. Proximal Independent Metropolis-Hastings

The motivation for Proximal-IMH is to provide an alternative to Latent-IMH that avoids ill-conditioning induced by squaring \mathbf{F} and bypasses sampling in the latent variable u , which can be high-dimensional, nonlinear, or degenerate in practice. Proximal-IMH instead proceeds in two steps:

$$\tilde{x} \sim \pi_a(x | y), \quad (3a)$$

$$x = \arg \min_x \|\mathbf{A}(x) - \tilde{\mathbf{A}}(\tilde{x})\|^2 + \beta\|x - \tilde{x}\|^2. \quad (3b)$$

3.1. Linear Input-Output Operator \mathbf{A}

When the forward operator \mathbf{A} is linear and full rank, the optimization problem Equation (3b) admits a closed-form solution:

$$x = \mathbf{K}\tilde{x}, \quad \mathbf{K} = (\mathbf{A}^\top \mathbf{A} + \beta \mathbf{I})^{-1}(\mathbf{A}^\top \tilde{\mathbf{A}} + \beta \mathbf{I}). \quad (4)$$

The resulting proposal distribution is the push-forward $\pi_p(\cdot | y) = \mathbf{K}_{\#}\pi_a(\cdot | y)$ and admits the density

$$\pi_p(x | y) \propto q\left(y - \tilde{\mathbf{A}}\mathbf{K}^{-1}x\right) p(\mathbf{K}^{-1}x). \quad (5)$$

Accordingly, the Metropolis–Hastings acceptance ratio takes the form

$$\min\left\{1, \frac{q(y - \mathbf{A}x') q(y - \tilde{\mathbf{A}}\tilde{x}_t) p(x') p(\tilde{x}_t)}{q(y - \tilde{\mathbf{A}}\tilde{x}') q(y - \mathbf{A}x_t) p(\tilde{x}') p(x_t)}\right\}, \quad (6)$$

where $\tilde{x}_t, \tilde{x}' \sim \pi_a(x | y)$, $x_t = \mathbf{K}\tilde{x}_t$ is the current state, and $x' = \mathbf{K}\tilde{x}'$ is the proposed state.

The operator \mathbf{K} can be equivalently expressed as

$$\mathbf{K} = \mathbf{I} + \mathbf{A}^\dagger(\tilde{\mathbf{A}} - \mathbf{A}), \quad (7)$$

where $\mathbf{A}^\dagger = (\mathbf{A}^\top \mathbf{A} + \beta \mathbf{I})^{-1} \mathbf{A}^\top$ is a regularized pseudoinverse of \mathbf{A} . Under this form of \mathbf{K} , the proposal mechanism of Proximal-IMH (Equations (3a) and (3b)) can be interpreted as a correction of an approximate posterior sample $\tilde{x} \sim \pi_a(x | y)$ via

$$x \leftarrow \tilde{x} + \mathbf{A}^\dagger(\tilde{\mathbf{A}}\tilde{x} - \mathbf{A}\tilde{x}). \quad (8)$$

Here, the term $\tilde{\mathbf{A}}\tilde{x} - \mathbf{A}\tilde{x}$ represents a correction of the observation residual induced by the approximate forward model, while the operator \mathbf{A}^\dagger maps this correction back into the parameter (i.e., x -) space.

Hyperparameter β . The regularization parameter β controls the trade-off between enforcing consistency with the exact forward model and stabilizing the correction around the approximate sample \tilde{x} . To balance these effects relative to the noise level, we choose $\beta = \Theta(\sigma^2)$, where σ^2 is the variance of the observational noise. This scaling prevents overfitting to noise while ensuring that the correction remains effective in mitigating operator mismatch. In particular, $\beta = \Theta(\sigma^2)$ is required in the KL-divergence analysis (Section 3.2) and for the mixing-time bounds of Proximal-IMH (Theorem 3.3). We further investigate the effect of β in the numerical experiments.

3.2. Comparison of Proposal Distributions

We compare the proposal distributions used in Approx-IMH, Latent-IMH, and Proximal-IMH against Exact posterior using the expected Kullback–Leibler (KL) divergence, where the expectation is taken with respect to the observation y . For Approx posterior, we define the expected KL divergence \mathbb{D}_a as

$$\mathbb{D}_a := 2 \mathbb{E}_y[\text{KL}(\pi_a(x | y) \| \pi(x | y))]. \quad (9)$$

The quantities \mathbb{D}_l and \mathbb{D}_p are defined analogously for Latent posterior and Proximal posterior, respectively.

Assumption 3.1. The prior is $p(x) = \mathcal{N}(\mathbf{0}, \mathbf{I})$ and the observational noise is $q(e) = \mathcal{N}(\mathbf{0}, \sigma^2 \mathbf{I})$.

Under Assumption 3.1, and assuming that the forward operators \mathbf{A} and $\tilde{\mathbf{A}}$ are full-rank, all posterior distributions appearing in our analysis are multivariate Gaussian (see Table 1).

Diagonal case. We first consider a simplified setting in which both \mathbf{F} and $\tilde{\mathbf{F}}$ are diagonal, with an identity observation operator $\mathbf{O} = [\mathbf{I} \ \mathbf{0}]$. Closed-form expressions for the corresponding expected KL divergences are given below.

Theorem 3.2 (Adapted from Proposition 3.3 in (Chen & Biros, 2026)). *Under Assumption 3.1, let $\mathbf{F}_{ii} = s_i$ and $\tilde{\mathbf{F}}_{ii} = \alpha_i s_i$ for $i \in [d]$. Define $\rho_i := \alpha_i^2 s_i^2 + \sigma^2 / s_i^2 + \sigma^2$ and $\zeta_i := 1 / (\alpha_i^2 s_i^2 + \sigma^2)$. Setting $\beta = \sigma^2$ in the Proximal proposal, the expected KL divergences are given by*

$$\begin{aligned} \mathbb{D}_a &= -d_y + \sum_{i=1}^{d_y} \frac{1}{\rho_i} + \log \rho_i + \zeta_i (\alpha_i - 1)^2 (\alpha_i s_i^2 - \sigma^2)^2 \frac{s_i^2}{\sigma^2}, \\ \mathbb{D}_l &= -d + \sum_{i=1}^{d_y} \left(\frac{\alpha_i^2}{\rho_i} + \log \frac{\rho_i}{\alpha_i^2} \right) + \sum_{i=d_y+1}^d \left(\alpha_i^2 + \log \frac{1}{\alpha_i^2} \right) \\ &\quad + \sum_{i=1}^{d_y} \zeta_i (\alpha_i^2 - 1)^2 s_i^2 \sigma^2. \\ \mathbb{D}_p &= -d_y + \sum_{i=1}^{d_y} \left(\rho_i + \log \frac{1}{\rho_i} \right) + \zeta_i (\alpha_i - 1)^2 s_i^2 \sigma^2. \end{aligned} \quad (10)$$

Let $\epsilon := |\alpha_i - 1|$ denote the perturbation magnitude. When ϵ is small, the leading-order behavior is given by

$$\begin{aligned} \mathbb{D}_a &\sim \epsilon^2 d_y + \epsilon^2 \sum_{i \in [d_y]} \frac{s_i^2}{\sigma^2}, & \mathbb{D}_l &\sim \epsilon^2 d + \epsilon^2 \sum_{i \in [d_y]} \frac{\sigma^2}{s_i^2}, \\ \mathbb{D}_p &\sim \epsilon^2 d_y + \epsilon^2 \sum_{i \in [d_y]} \frac{\sigma^2}{s_i^2}. \end{aligned} \quad (11)$$

In most applications of interest, $\sum_i s_i^2 / \sigma^2 \gg \sum_i \sigma^2 / s_i^2$, which implies that \mathbb{D}_a typically dominates both \mathbb{D}_l and \mathbb{D}_p . Moreover, while \mathbb{D}_l and \mathbb{D}_p exhibit a comparable mean mismatch, the covariance mismatch of \mathbb{D}_p is generally smaller, especially when $d \gg d_y$.

General case. Beyond the diagonal case, we study the sensitivity of \mathbb{D}_a , \mathbb{D}_l , and \mathbb{D}_p in a more general setting. We consider $\mathbf{F} = \mathbf{V}\mathbf{S}\mathbf{V}^\top$ and its approximation as $\tilde{\mathbf{F}} = \mathbf{V}\tilde{\mathbf{S}}\mathbf{V}^\top$, where \mathbf{V} is a unitary matrix obtained from the singular value decomposition of a random matrix. The diagonal matrix \mathbf{S} has entries $\{1/i^2\}_{i \in [d]}$, while $\tilde{\mathbf{S}}$ has entries $\{\alpha_i/i^2\}_{i \in [d]}$. The observation operator \mathbf{O} is taken to be a full-rank random

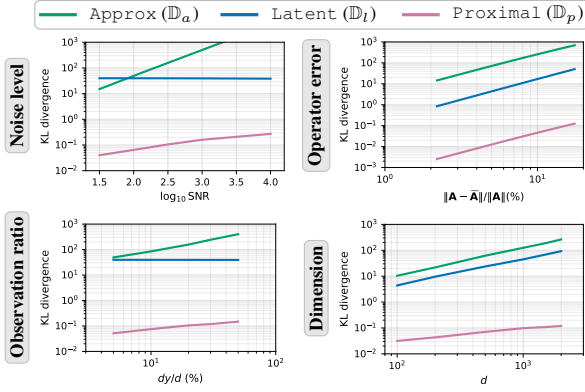


Figure 1. Sensitivity of the expected KL divergence of the Approx, Latent, and Proximal proposals (relative to the Exact posterior) for different noise levels, operator errors, observation ratios, and dimensions. Details of the experimental setup are given in Table 2.

matrix. We evaluate the expected KL divergence by varying four factors: the noise level, the magnitude of the operator perturbation, the observation ratio (d_y/d), and the problem dimension. The experimental design for these sensitivity studies is summarized in Table 2, and the corresponding results are reported in Figure 1. In all regimes tested, \mathbb{D}_p consistently achieves substantially lower values—often by orders of magnitude—than both \mathbb{D}_a and \mathbb{D}_l .

3.3. Mixing Time of IMH Schemes

We now compare the convergence behavior of different IMH methods in terms of mixing time. The mixing time of the APPROX-IMH chain under a warm start $\pi_a(x | y)$ is defined as

$$\tau_{mix}^a(\epsilon) := \inf \{n \in \mathbb{N} : \|\pi_a P_a^n - \pi\|_{TV} \leq \epsilon\}, \quad (12)$$

where P_a denotes the IMH transition kernel with the proposal distribution $\pi_a(x | y)$, and $\|\cdot\|_{TV}$ denotes the total variation distance. Analogously, we define the mixing times for Latent-IMH and Proximal-IMH as $\tau_{mix}^l(\epsilon)$ and $\tau_{mix}^p(\epsilon)$, respectively. The theorem below establishes explicit mixing-time bounds for the three IMH schemes under the assumption of a linear forward model and a log-concave prior.

Theorem 3.3 (Mixing time for three IMH schemes.). *Assume that the prior density $p(x)$ is log-concave and that there exist constants $L, m > 0$ such that $-\log p(x)$ is L -smooth and m -strongly convex on \mathbb{R}^d . Assume further that the noise density $q(e)$ is Gaussian with variance σ^2 , and that the forward operator \mathbf{F} and its approximation $\tilde{\mathbf{F}}$ are linear and invertible (as required by the Latent-IMH proposal). In Proximal-IMH, set the regularization parameter $\beta = \Theta(\sigma^2)$. Let $\Delta\mathbf{A} := \tilde{\mathbf{A}} - \mathbf{A}$. Then the mixing times of Approx-IMH, Latent-IMH, and Proximal-IMH*

satisfy

$$\tau_{mix}^a(\epsilon) \sim \frac{d}{m^2} \frac{\|\mathbf{A}^\top \Delta\mathbf{A}\|^2}{\sigma^4} \log(1/\epsilon), \quad (13)$$

$$\tau_{mix}^l(\epsilon) \sim \frac{dL^2}{m^2} \left\| \mathbf{I} - \tilde{\mathbf{F}}^{-1}\mathbf{F} \right\|^2 \log(1/\epsilon), \quad (14)$$

$$\tau_{mix}^p(\epsilon) \sim \frac{dL^2}{m^2} \left\| \mathbf{I} - \mathbf{K}^{-1} \right\|^2 \log(1/\epsilon). \quad (15)$$

Proof sketch. The result follows from the general mixing-time bound in Theorem A.3, which reduces the analysis to bounding local Lipschitz constants of the log-weight functions associated with each IMH proposal. The detailed proof is provided in Section A.2. For APPROX-IMH, the log-weight admits a quadratic form involving the operator mismatch $\Delta\mathbf{A}$, resulting in a Lipschitz constant proportional to $\|\mathbf{A}^\top \Delta\mathbf{A}\|/\sigma^2$. For LATENT-IMH, smoothness of the negative log-prior implies that the Lipschitz constant is controlled by $\|\mathbf{I} - \tilde{\mathbf{F}}^{-1}\mathbf{F}\|$. For PROXIMAL-IMH, the correction operator \mathbf{K}^{-1} introduces additional regularization, and choosing $\beta = \Theta(\sigma^2)$ ensures dependence on $\|\mathbf{I} - \mathbf{K}^{-1}\|$. Substituting these bounds into Theorem A.3 yields the stated scaling of the mixing times. \square

As shown in Theorem 3.3, the mixing time of APPROX-IMH scales unfavorably with the signal-to-noise ratio $\|\mathbf{A}\|/\sigma^2$, which is typically large in inverse problems. Both LATENT-IMH and PROXIMAL-IMH remove this explicit dependence, but differ in how operator errors are amplified.

For LATENT-IMH, the term $\|\mathbf{I} - \tilde{\mathbf{F}}^{-1}\mathbf{F}\|$ depends on the full perturbation $\Delta\mathbf{F} = \tilde{\mathbf{F}} - \mathbf{F}$ and is amplified by the conditioning of $\tilde{\mathbf{F}}$ through $\|\tilde{\mathbf{F}}^{-1}\|$, which can become large even for small $\|\Delta\mathbf{F}\|$. In contrast, PROXIMAL-IMH depends only on the observable perturbation $\Delta\mathbf{A} = \mathbf{O}\Delta\mathbf{F}$, filtered through the regularized pseudoinverse \mathbf{A}^\dagger in $\mathbf{K} = \mathbf{I} + \mathbf{A}^\dagger(\tilde{\mathbf{A}} - \mathbf{A})$. As a result, the mixing behavior of PROXIMAL-IMH is more robust to operator perturbations.

A sharper comparison can be obtained in the diagonal setting introduced in the previous section for the KL-divergence comparison. In that case, one can show that

$$\|\mathbf{I} - \mathbf{K}^{-1}\| \leq \|\mathbf{I} - \tilde{\mathbf{F}}^{-1}\mathbf{F}\|, \quad (16)$$

with equality attained only when $\mathbf{F} = \tilde{\mathbf{F}}$.

3.4. Nonlinear Operator

We now extend PROXIMAL-IMH to nonlinear forward problems. Recall the optimization problem Equation (3b): given a sample $\tilde{x} \sim \pi_a(x | y)$ from the approximate posterior, it is expected that the proposal x will remain close to \tilde{x} while reducing the data misfit. In the nonlinear least-squares setting, Gauss–Newton methods are known to achieve local

quadratic convergence when the residual is small, making them a natural choice for this correction step.

Specifically, we consider a single Gauss–Newton step applied to Equation (3b),

$$x \leftarrow GN(\tilde{x}) := \tilde{x} - (\mathbf{J}(\tilde{x})^\top \mathbf{J}(\tilde{x}) + \beta \mathbf{I})^{-1} \mathbf{J}(\tilde{x})^\top r(\tilde{x}), \quad (17)$$

where $r(\tilde{x}) = \mathbf{A}(\tilde{x}) - \tilde{\mathbf{A}}(\tilde{x})$ denotes the residual and $\mathbf{J}(\tilde{x})$ is the Jacobian of $\mathbf{A}(\cdot)$ evaluated at \tilde{x} . When \mathbf{A} is linear, a single Gauss–Newton step recovers the exact solution given in Equation (4).

Under this construction, the Proximal-IMH proposal induced by one Gauss–Newton step can be expressed as a pushforward distribution,

$$\pi_p(x | y) = \pi_a(\tilde{x} | y) |\det \mathbf{J}_{GN}(\tilde{x})|^{-1}, \quad (18)$$

where $\tilde{x} = GN^{-1}(x)$ and $\mathbf{J}_{GN}(\tilde{x})$ denotes the Jacobian of the Gauss–Newton map $GN(\cdot)$ at \tilde{x} . The corresponding Metropolis–Hastings acceptance ratio is

$$\min \left\{ 1, \frac{\pi(x' | y) \pi_a(\tilde{x}_t | y) |\det \mathbf{J}_{GN}(\tilde{x}')|}{\pi(x_t | y) \pi_a(\tilde{x}' | y) |\det \mathbf{J}_{GN}(\tilde{x}_t)|} \right\}, \quad (19)$$

where $\tilde{x}_t, \tilde{x}' \sim \pi_a(x | y)$ and $x_t = GN(\tilde{x}_t)$ denote the current state, $x' = GN(\tilde{x}')$ is the proposed state.

Compared with the linear acceptance ratio in Equation (6), the only additional term is the Jacobian determinant ratio. Since the Gauss–Newton update Equation (17) represents a small, local correction around \tilde{x} , we expect this determinant ratio to be close to one in practice and thus to have a negligible impact on the acceptance ratio.

To illustrate this setting concretely, we consider a nonlinear model $y = \mathbf{A}G(x) + e$, where \mathbf{A} is a full-rank matrix and G is a nonlinear mapping. We assume a Gaussian prior on x and additive Gaussian noise $e \sim \mathcal{N}(0, \sigma^2 \mathbf{I})$. This model is standard in inverse problems with deep generative model-informed priors, including generative adversarial networks (GANs), variational autoencoders (VAEs), and normalizing flows, where x represents the latent variable and G corresponds to the decoder or generator implemented by a neural network.

Consider a small perturbation $\Delta \mathbf{A} = \tilde{\mathbf{A}} - \mathbf{A} = \delta \mathbf{A}$ for some $\delta \in (0, 1)$. For arbitrary points \tilde{x}_1 and \tilde{x}_2 , we have

$$\log \frac{|\det \mathbf{J}_{GN}(\tilde{x}_1)|}{|\det \mathbf{J}_{GN}(\tilde{x}_2)|} = \sum_{i \in [d_x]} \log \frac{1 - \delta \lambda_{1,i} / (\lambda_{1,i} + \beta)}{1 - \delta \lambda_{2,i} / (\lambda_{2,i} + \beta)}, \quad (20)$$

where $\{\lambda_{1,i}\}$ and $\{\lambda_{2,i}\}$ denote the eigenvalues (in descending order) of $\mathbf{J}^\top(\tilde{x}_1)\mathbf{J}(\tilde{x}_1)$ and $\mathbf{J}^\top(\tilde{x}_2)\mathbf{J}(\tilde{x}_2)$, respectively. Since $\beta = \Theta(\sigma^2)$, when $\lambda_{1,i}, \lambda_{2,i} \gg \beta$ the corresponding

terms are negligible. When $\lambda_{1,i}$ and $\lambda_{2,i}$ are comparable to β , the log ratio is determined by their difference but remains uniformly bounded by $\log(1 - \delta)^{-1}$.

In our nonlinear implementation, we therefore neglect the Jacobian determinant ratio when computing the acceptance probability. We further examine the validity of this approximation in the numerical experiments. For specific applications, however, we recommend monitoring the scale of this ratio to determine whether its contribution can be safely ignored.

4. Numerical Experiments

We design numerical experiments to compare Proximal-IMH with existing IMH schemes, to evaluate its nonlinear extension, and to assess consistency with theory. Performance is measured using acceptance rates, relative mean error, and relative componentwise second-moment error. In all experiments, the observational noise is Gaussian and the noise-to-signal ratio $\|e\|/\|y\|$ is controlled to be between 15% and 20%. We additionally include the No-U-Turn Sampler (NUTS) as a baseline to provide a reference for sampling quality and computational efficiency. Because NUTS requires repeated evaluations of the exact forward operator, it is used primarily as a benchmark and is not considered a directly comparable low-cost alternative. We present a linear forward model test in Section 4.1 and two nonlinear forward model tests in Sections 4.2 and 4.3.

4.1. Bimodal Test.

We consider the following prior distribution

$$p(x) \propto \exp \left(-\frac{1}{2} \|x\|^2 - \tau (w^\top x - c)^2 (w^\top x + c)^2 \right), \quad (21)$$

where $x \in \mathbb{R}^{200}$, $w \in \mathbb{R}^{200}$ satisfies $\|w\| = 1$, and we set $c = 2$ and $\tau = 0.3$. This prior is bimodal along the projection direction $w^\top x$. We visualize the marginal prior distribution of $w^\top x$ in Figure 9.

We construct $\mathbf{A} = \mathbf{O}\mathbf{F}$ with $\mathbf{F} = \mathbf{V}\mathbf{S}\mathbf{V}^\top$, where \mathbf{V} is orthogonal, \mathbf{S} is diagonal with $\mathbf{S}_{ii} = 1/i$, $d_y = 50$, and $\mathbf{O} \in \mathbb{R}^{d_y \times d_x}$ is well conditioned.

We consider three different constructions of the approximate forward operator $\tilde{\mathbf{F}}$, with $\tilde{\mathbf{A}} = \mathbf{O}\tilde{\mathbf{F}}$:

- **Test I (Multiplicative spectral perturbation).** $\tilde{\mathbf{F}} = \mathbf{V}\tilde{\mathbf{S}}\mathbf{V}^\top$, where $\tilde{\mathbf{S}}$ is diagonal with entries $\tilde{\mathbf{S}}_{ii} = \alpha_i \mathbf{S}_{ii}$, $\alpha_i \sim \mathcal{U}[\alpha_-, \alpha_+]$, with $\alpha_- \in (0, 1)$ and $\alpha_+ > 1$.
- **Test II (Additive low-rank perturbation).** We define $\tilde{\mathbf{F}} = \mathbf{F} + \epsilon \mathbf{U}_1 \mathbf{U}_2^\top$, where $\mathbf{U}_1, \mathbf{U}_2 \in \mathbb{R}^{d_x \times 5}$ have i.i.d. standard normal entries.

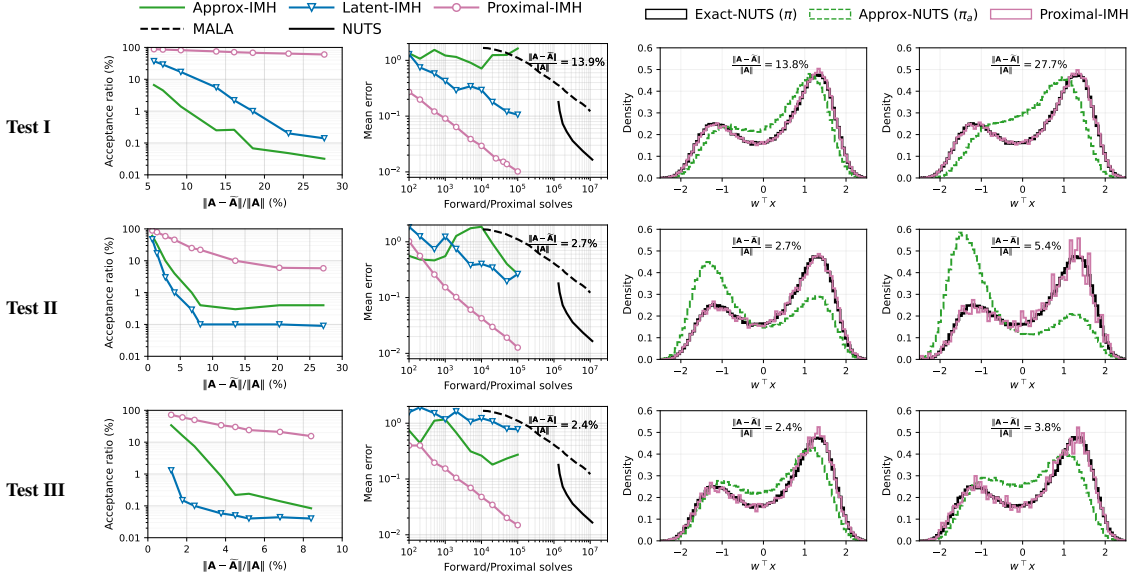


Figure 2. Comparison of sampling performance in the bimodal test. Rows correspond to Tests I–III. From left to right, panels show Metropolis–Hastings acceptance rates for three IMH methods, convergence of the relative mean error for the IMH methods together with NUTS and MALA, and histograms of the projected samples $w^\top x$ for two levels of operator error. In the histogram panels, Approx-NUTS denotes samples drawn from the Approx posterior $\pi_a(x | y)$. For Proximal-IMH, we set $\beta = \sigma^2$. Results in the left panel are averaged over 5 independent trials for each method.

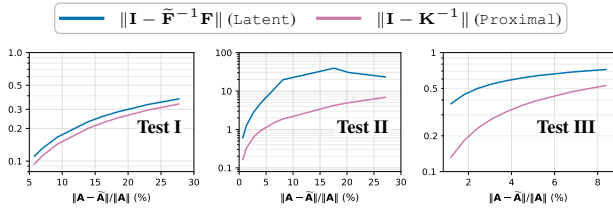


Figure 3. Operator discrepancy in the bimodal test. The quantities $\|\mathbf{I} - \tilde{\mathbf{F}}^{-1}\mathbf{F}\|$ and $\|\mathbf{I} - \mathbf{K}^{-1}\|$ are reported for Latent-IMH and Proximal-IMH, respectively, where \mathbf{K} is defined in Equation (7). For Proximal-IMH, the hyperparameter is set to $\beta = \sigma^2$.

- **Test III (Low-rank approximation).** We define $\tilde{\mathbf{F}} = \mathbf{V}\tilde{\mathbf{S}}\mathbf{V}^\top$, where $\tilde{\mathbf{S}}$ is obtained by setting $\tilde{S}_{ii} = S_{ii}$ if $S_{ii} > \alpha$ and $\tilde{S}_{ii} = 0$ otherwise, for a threshold $\alpha > 0$.

Figure 2 compares the sampling performance of different methods in the bimodal test between Tests I–III. Across Tests I–III, Proximal-IMH consistently outperforms Approx-IMH and Latent-IMH, achieving substantially higher acceptance rates, particularly as $\|\mathbf{A} - \tilde{\mathbf{A}}\|/\|\mathbf{A}\|$ increases.

In Test II, the additive low-rank perturbation $\Delta\mathbf{F}$ significantly degrades the conditioning of \mathbf{F} , leading to amplified inverse-operator errors. To interpret this behavior, we report in Figure 3 the operator discrepancy terms that appear in the mixing-time bounds Equations (14) and (15). Although the theoretical analysis in Section 3.3 assumes log-concave

targets and the bimodal prior used here violates this assumption, the same operator-norm quantities still govern proposal sensitivity. In particular, the filtered error $\|\mathbf{I} - \mathbf{K}^{-1}\|$ remains stable under perturbations that cause $\|\mathbf{I} - \tilde{\mathbf{F}}^{-1}\mathbf{F}\|$ to grow rapidly, which explains the improved robustness of Proximal-IMH relative to Latent-IMH.

From the convergence plots in Figure 2, Proximal-IMH converges significantly faster than the other IMH variants and achieves accuracy comparable to NUTS while using independent proposals. MALA converges slowly in this setting due to both the bimodal posterior and the large smoothness constant of the negative log-posterior, which scales as $L + \|\mathbf{A}\|^2/\sigma^2$ and leads to an unfavorable mixing-time dependence (Dwivedi et al., 2019).

The right columns show histograms of the projected samples $w^\top x$ for two representative perturbation levels. Approx-NUTS, which samples the approximate posterior $\pi_a(x | y)$, exhibits biased mode weights, whereas Proximal-IMH accurately captures both modes in all tests.

Finally, Figure 4 presents the effect of the hyperparameter β in Proximal-IMH. In all tests, higher acceptance rates correlate with lower relative mean errors, with optimal performance consistently achieved near $\beta = \sigma^2$. Performance degrades noticeably for $\beta > 2\sigma^2$, indicating increased sensitivity to over-regularization.

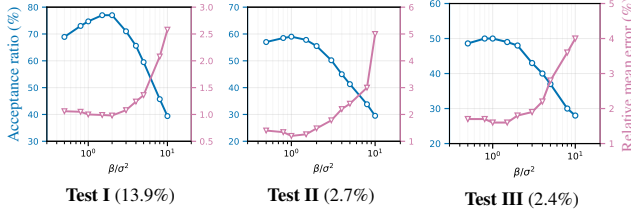


Figure 4. Effect of β on Proximal-IMH in the bimodal test. Values in parentheses represent $\|\mathbf{A} - \tilde{\mathbf{A}}\|/\|\mathbf{A}\|$. Blue curves show acceptance rates (left y-axis), and pink curves show relative mean errors after 10^5 MH steps (right y-axis).

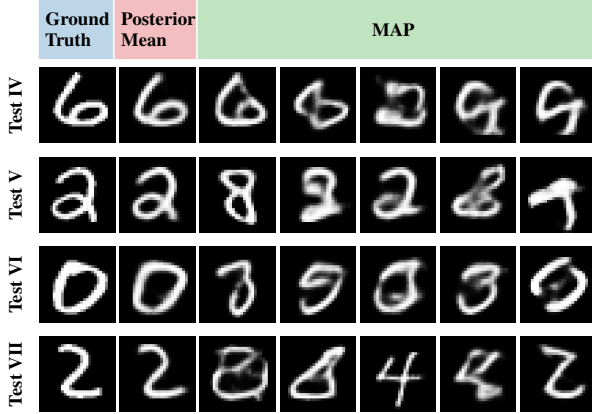


Figure 5. Ground truth, posterior mean and MAP estimates for the MNIST inverse problem in Tests IV–VII. The MAP estimates are obtained from different random initial guesses for the optimization problem. We observe that in several cases the reconstructed MAP point is wrong. This is due to the nonconvexity of solving for a MAP point.

4.2. MNIST test.

We consider an inverse imaging problem with the forward model $y = \mathbf{A}x + e$, where x denotes the image in pixel space, \mathbf{A} is a full-rank linear operator, and y is the observed signal. As a prior, we use the decoder of a variational autoencoder (VAE) trained on the MNIST dataset (LeCun et al., 1998). Specifically, let $G(\cdot)$ denote the decoder mapping latent variables to images in the pixel space. The forward model in latent space is then given by $y = \mathbf{A}G(z) + e$. In our experiments, we set $d_z = 128$, $d_x = 784$, and $d_y = 100$. We focus on sampling the posterior distribution in the latent space:

$$\pi(z | y) \propto \exp\left(-\frac{1}{2\sigma^2}\|\mathbf{A}G(z) - y\|^2 - \frac{1}{2}\|z\|^2\right). \quad (22)$$

We randomly select digits from the MNIST test dataset, which were not seen during VAE training, and generate observations through $y = \mathbf{A}x + e$. We consider two types of exact operators \mathbf{A} and approximations $\tilde{\mathbf{A}}$:

- **Tests IV and V:** The operators \mathbf{A} and $\tilde{\mathbf{A}}$ are constructed

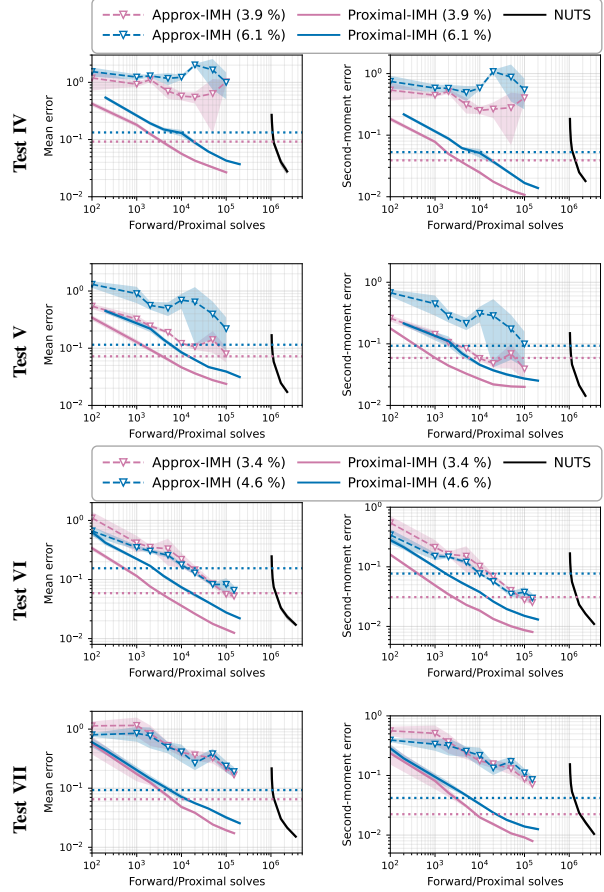


Figure 6. Sampling performance on MNIST imaging inverse problems: convergence of the relative mean error and relative second-moment error for different sampling methods. Dashed lines indicate the bias induced by the Approx posterior $\pi_a(x | y)$. For Proximal-IMH, we set $\beta = \sigma^2$. Results in the convergence plots are reported over 5 independent trials.

in the same manner as in Test I. The resulting operator \mathbf{A} has condition number $\kappa(\mathbf{A}) \approx 60$.

- **Tests VI and VII (linearized Helmholtz operator):** The operator \mathbf{A} is constructed using a linearized Helmholtz operator based on the Born Approximation (Colton & Kress, 1998) on a fine grid (100×100). The approximation $\tilde{\mathbf{A}}$ is constructed on coarser grids (35×35 or 20×20). The operator \mathbf{A} has condition number $\kappa(\mathbf{A}) \approx 420$. Details of the construction procedure are provided in Section C.3.

Figure 5 shows the ground truth, posterior means, and maximum-a-posteriori (MAP) estimates for the MNIST inverse problem. MAP solutions are obtained by directly minimizing the negative logarithmic posterior defined in Equation (22), using the Adam optimizer with a sufficiently large number of iterations to ensure convergence. As illustrated in the figure, the resulting MAP estimates display substantial variability across runs, reflecting the nonconvexity of the posterior landscape. In contrast, the posterior

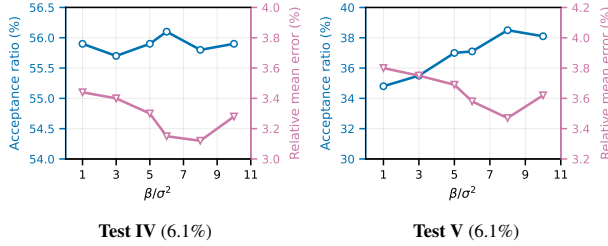


Figure 7. Effect of the hyperparameter β on Proximal-IMH in the inverse problem in MNIST. Values in parentheses represent $\|\mathbf{A} - \tilde{\mathbf{A}}\|/\|\mathbf{A}\|$. Blue curves show acceptance rates (left y-axis), and pink curves show relative mean errors after 10^5 MH steps (right y-axis). The results are not sensitive to β .

means reported in Figure 6 achieve noticeably smaller reconstruction errors relative to the ground truth.

We further report convergence results for Approx-IMH, Proximal-IMH, and NUTS in terms of the relative mean error and the relative componentwise second moment error; Proximal-IMH uses a single Gauss–Newton step. Compared to Approx posterior, Proximal-IMH exhibits lower error with faster convergence, reduced variability across trials, and robustness to different observation realizations.

Figure 7 illustrates the effect of β on Proximal-IMH. Consistent with bimodal experiments (Figure 4), higher acceptance rates are associated with smaller relative mean errors, but performance in this test is largely insensitive to β , with a mean error variance below 0.4%. We further examine the variability of the Jacobian determinant associated with a single Gauss–Newton correction in Figure 11.

4.3. Nonlinear Helmholtz test.

We consider a nonlinear inverse problem arising from acoustic scattering governed by the Helmholtz equation. The unknown medium x is represented on a 32×32 grid, while the wavefield is discretized on a finer grid 128×128 . We consider 4 independent source terms. The forward operator $\mathbf{A}_i(x)$ is defined implicitly by solving a Helmholtz equation with homogeneous Neumann boundary conditions (see Section C.4 for details). The Helmholtz operator is nonlinear with respect to the scatterer properties. Assuming independent observations, the negative log-posterior $-\log \pi(x | \{y_i\})$ (up to an additive constant) is

$$\frac{1}{2\sigma^2} \sum_{i=1}^4 \|y_i - \mathbf{A}_i(x)\|^2 + TV_\epsilon(x), \quad (23)$$

where $TV_\epsilon(x)$ denotes a smoothed total-variation prior.

To construct an approximate forward model, we solve the Helmholtz equation on a coarser 64×64 grid. All linear systems arising in the forward and adjoint solves are com-

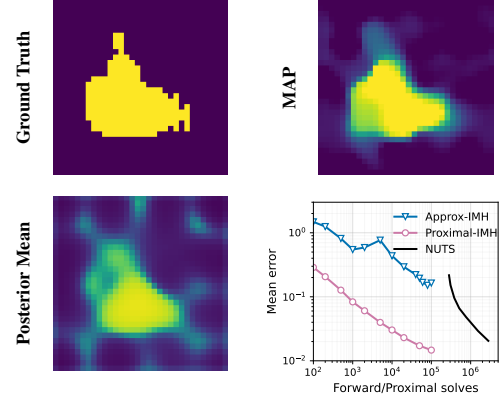


Figure 8. Nonlinear Helmholtz inverse problem. Ground truth, MAP estimate, and posterior mean for the acoustic scattering test, together with convergence of the relative mean error.

puted using GMRES with a Neumann–DCT preconditioner; implementation details are provided in Section C.4.

Figure 8 shows the ground truth, the MAP estimate, and the posterior mean. The MAP estimate is closer to the ground truth because the smoothed TV prior is weakly informative, allowing the likelihood to dominate the posterior; this observation is further corroborated by Figure 13 in the appendix, where the corresponding wavefield solutions u_i for the ground truth, MAP, and posterior mean are nearly indistinguishable. From the convergence results in Figure 8, Proximal-IMH consistently outperforms Approx-IMH and achieves accuracy comparable to NUTS, while retaining the computational advantages of independent proposals.

5. Conclusion

We introduced Proximal-IMH, an independence Metropolis–Hastings sampler for inverse problems with approximate forward operators. Proximal-IMH generates global proposals by correcting samples from an approximate posterior through a stable optimization step. For linear forward models, we showed that Proximal-IMH achieves smaller expected KL divergence and faster mixing than existing IMH schemes under suitable regularity assumptions. Numerical experiments on multimodal, imaging, and nonlinear PDE-based inverse problems consistently confirm improved acceptance rates, convergence, and accuracy.

Limitations. Theoretical guarantees are derived under linear forward models and regularity assumptions on the prior, while the nonlinear extension relies on local Gauss–Newton corrections and neglects Jacobian terms in practice. Performance also depends on the quality of the approximate operator $\tilde{\mathbf{F}}$ and the choice of the regularization parameter β in some cases.

Impact Statement

This paper aims to advance the field of Machine Learning. While our work may have various societal impacts, none require specific mention here.

References

- Arridge, S. R. and Schotland, J. C. Optical tomography: forward and inverse problems. *Inverse Problems*, 25(12):123010, 2009.
- Biegler, L., Biros, G., Ghattas, O., Heinkenschloss, M., Keyes, D., Mallick, B., Tenorio, L., van Bloemen Waanders, B., Willcox, K., and Marzouk, Y. *Large-scale inverse problems and quantification of uncertainty*, volume 712. Wiley Online Library, 2010.
- Chen, Y. and Biros, G. Latent-IMH: Efficient Bayesian inference for inverse problems with approximate operators. *arXiv preprint*, 2026.
- Cohen, M. B., Kyng, R., Miller, G. L., Pachocki, J. W., Peng, R., Rao, A. B., and Xu, S. C. Solving sdd linear systems in nearly $m \log^{1/2} n$ time. In *Proceedings of the forty-sixth annual ACM symposium on Theory of computing*, pp. 343–352, 2014.
- Colton, D. and Kress, R. *Inverse Acoustic and Electromagnetic Scattering Theory, 2nd Edition*. Applied Mathematical Sciences. Springer, 1998.
- Dwivedi, R., Chen, Y., Wainwright, M. J., and Yu, B. Log-concave sampling: Metropolis-hastings algorithms are fast. *Journal of Machine Learning Research*, 20(183):1–42, 2019.
- Epstein, C. L. *Introduction to the mathematics of medical imaging*. SIAM, 2007.
- Ghattas, O. and Willcox, K. Learning physics-based models from data: perspectives from inverse problems and model reduction. *Acta Numerica*, 30:445–554, 2021.
- Girolami, M. and Calderhead, B. Riemann manifold Langevin and Hamiltonian Monte Carlo methods. *Journal of the Royal Statistical Society: Series B (Statistical Methodology)*, 73(2):123–214, 2011.
- Henson, V. E. and Yang, U. M. Boomeramg: a parallel algebraic multigrid solver and preconditioner. *Appl. Numer. Math.*, 41(1):155–177, 2002. ISSN 0168-9274.
- Herrmann, L., Schwab, C., and Zech, J. Neural and spectral operator surrogates: unified construction and expression rate bounds. *Advances in Computational Mathematics*, 50(4):72, 2024.
- Hoffman, M. D., Gelman, A., et al. The No-U-Turn sampler: adaptively setting path lengths in Hamiltonian Monte Carlo. *Journal of Machine Learning Research*, 15(1):1593–1623, 2014.
- Kaipio, J. and Somersalo, E. *Statistical and computational inverse problems*, volume 160. Springer Science & Business Media, 2006.
- Kaipio, J. P., Kolehmainen, V., Somersalo, E., and Vauhkonen, M. Statistical inversion and Monte Carlo sampling methods in electrical impedance tomography. *Inverse Problems*, 16(5):1487–1522, 2000.
- LeCun, Y., Bottou, L., Bengio, Y., and Haffner, P. Gradient-based learning applied to document recognition. *Proceedings of the IEEE*, 86(11):2278–2324, 1998.
- Liang, D., Cheng, J., Ke, Z., and Ying, L. Deep magnetic resonance image reconstruction: Inverse problems meet neural networks, 2020.
- Papamakarios, G., Nalisnick, E., Rezende, D. J., Mohamed, S., and Lakshminarayanan, B. Normalizing flows for probabilistic modeling and inference. *Journal of Machine Learning Research*, 22(57):1–64, 2021.
- Peherstorfer, B., Willcox, K., and Gunzburger, M. Survey of multifidelity methods in uncertainty propagation, inference, and optimization. *SIAM Review*, 60(3):550–591, 2018. doi: 10.1137/16M1082469. URL <https://doi.org/10.1137/16M1082469>.
- Roberts, G. O. and Tweedie, R. L. Exponential convergence of Langevin distributions and their discrete approximations. 1996.
- Saratoon, T., Tarvainen, T., Cox, B., and Arridge, S. A gradient-based method for quantitative photoacoustic tomography using the radiative transfer equation. *Inverse Problems*, 29(7):075006, 2013.
- Song, Y., Shen, L., Xing, L., and Ermon, S. Solving inverse problems in medical imaging with score-based generative models. *arXiv preprint arXiv:2111.08005*, 2021.
- Spantini, A., Solonen, A., Cui, T., Martin, J., Tenorio, L., and Marzouk, Y. Optimal low-rank approximations of bayesian linear inverse problems. *SIAM Journal on Scientific Computing*, 37(6):A2451–A2487, 2015.
- Tarantola, A. *Inverse problem theory and methods for model parameter estimation*. Society for Industrial and Applied Mathematics (SIAM), Philadelphia, PA, 2005. ISBN 0-89871-572-5.
- Van der Vorst, H. A. *Iterative Krylov methods for large linear systems*. Number 13. Cambridge University Press, 2003.

Vogel, C. *Computational methods for inverse problems*,
volume 23. SIAM, 2002.

A. Proofs of Main Results

A.1. Proof of Theorem 3.2

Under the Gaussian setting, the expected KL divergence \mathbb{D}_a admits the following closed-form expression:

$$\begin{aligned} \mathbb{D}_a = & \underbrace{\log \frac{|\Sigma|}{|\Sigma_a|} + \text{Tr}(\Sigma^{-1}\Sigma_a) - d}_{\text{covariance mismatch}} \\ & + \underbrace{\frac{1}{\sigma^2} \|\mathbf{A}\Delta_a\mathbf{A}\|_F^2 + \sigma^2 \|\Delta_a\|_F^2 + 2\|\Delta_a\mathbf{A}\|_F^2}_{\text{mean mismatch}}, \end{aligned} \quad (24)$$

where $\Delta_a := \mathbf{A}_a^\dagger - \mathbf{A}^\dagger$. The explicit forms of Σ , Σ_a , \mathbf{A}^\dagger , and \mathbf{A}_a^\dagger are given in Table 1.

The expressions for \mathbb{D}_l and \mathbb{D}_p follow the same structure as Equation (24), with $(\mathbf{A}_a^\dagger, \Sigma_a)$ replaced by $(\mathbf{A}_l^\dagger, \Sigma_l)$ and $(\mathbf{A}_p^\dagger, \Sigma_p)$, respectively.

Proof of Theorem 3.2. The expressions for \mathbb{D}_a and \mathbb{D}_l have been proved in Proposition 3.3 in (Chen & Biros, 2026). We only need to prove the expression for \mathbb{D}_p here.

$$\mathbb{D}_p = \log \frac{|\Sigma|}{|\Sigma_p|} + \text{Tr}(\Sigma^{-1}\Sigma_p) - d + \frac{1}{\sigma^2} \|\mathbf{A}\Delta_p\mathbf{A}\|_F^2 + \sigma^2 \|\Delta_p\|_F^2 + 2\|\Delta_p\mathbf{A}\|_F^2, \quad (25)$$

where Σ and Σ_p are the covariances of Exact posterior and Proximal posterior, and $\Delta_p := \mathbf{A}_p^\dagger - \mathbf{A}^\dagger$ is the pseudo-inverse difference.

By the diagonal assumptions of \mathbf{F} , $\tilde{\mathbf{F}}$ and \mathbf{O} , we have $\mathbf{A}, \tilde{\mathbf{A}} \in \mathbb{R}^{d_y \times d}$ are matrices with zero elements except for:

$$\mathbf{A}_{ii} = s_i, \quad \tilde{\mathbf{A}}_{ii} = \alpha_i s_i, \quad \forall i \in [d_y]. \quad (26)$$

By the formulations listed in Table 1, $\mathbf{A}^\dagger, \mathbf{A}_a^\dagger, \mathbf{A}_p^\dagger \in \mathbb{R}^{d \times d_y}$ have all zero entries except for:

$$\mathbf{A}_{ii}^\dagger = \frac{s_i}{s_i^2 + \sigma^2}, \quad (\mathbf{A}_a^\dagger)_{ii} = \frac{\alpha_i s_i}{\alpha_i^2 s_i^2 + \sigma^2}, \quad (\mathbf{A}_p^\dagger)_{ii} = \frac{\alpha_i^2 s_i^3 + \sigma^2}{(s_i^2 + \sigma^2)(\alpha_i^2 s_i^2 + \sigma^2)}, \quad \forall i \in [d_y]. \quad (27)$$

Then $\Delta_p \in \mathbb{R}^{d \times d_y}$ is matrix with zero elements except for:

$$(\Delta_p)_{ii} = (\mathbf{A}_p^\dagger)_{ii} - \mathbf{A}_{ii}^\dagger = \frac{\sigma^2 s_i (\alpha_i - 1)}{(\alpha_i^2 s_i^2 + \sigma^2)(s_i^2 + \sigma^2)}, \quad \forall i \in [d_y]. \quad (28)$$

In addition, the covariance of the posterior $\Sigma, \Sigma_p \in \mathbb{R}^{d \times d}$ are diagonal matrices with diagonals as

$$\begin{cases} \Sigma_{ii} = \frac{\sigma^2}{s_i^2 + \sigma^2}, & (\Sigma_p)_{ii} = \frac{\sigma^2 \rho_i}{s_i^2 + \sigma^2}, & i \leq d_y, \\ \Sigma_{ii} = 1, & (\Sigma_p)_{ii} = 1, & i > d_y. \end{cases} \quad (29)$$

Thus, for the covariance mismatch of Equation (25), we have

$$\log \frac{|\Sigma|}{|\Sigma_p|} = \sum_{i \in [d_y]} \log \frac{1}{\rho_i}, \quad \text{Tr}(\Sigma^{-1}\Sigma_p) = \sum_{i \in [d_y]} \rho_i + d - d_y. \quad (30)$$

Based on Equation (28), we have

$$(\mathbf{A}\Delta_p)_{ii} = \frac{\sigma^2 s_i^2 (\alpha_i - 1)}{(\alpha_i^2 s_i^2 + \sigma^2)(s_i^2 + \sigma^2)} \quad (31)$$

Define $\psi_i = (\alpha_i^2 s_i^2 + \sigma^2)(s_i^2 + \sigma^2)$, we have formulations for the mean mismatch terms in Equation (25):

$$\frac{1}{\sigma^2} \|\mathbf{A}\Delta_p\mathbf{A}\|_F^2 = \sum_{i \in [d_y]} \frac{\sigma^2 s_i^6 (\alpha_i - 1)^2}{\psi_i^2}, \quad \sigma^2 \|\Delta_p\|_F^2 = \sum_{i \in [d_y]} \frac{\sigma^6 s_i^2 (\alpha_i - 1)^2}{\psi_i^2}, \quad 2\|\Delta_p\mathbf{A}\|_F^2 = \sum_{i \in [d_y]} \frac{2\sigma^4 s_i^4 (\alpha_i - 1)^2}{\psi_i^2}. \quad (32)$$

Thus, the mean mismatch term is

$$\frac{1}{\sigma^2} \|\mathbf{A}\Delta_p\mathbf{A}\|_F^2 + \sigma^2 \|\Delta_p\|_F^2 + 2\|\Delta_p\mathbf{A}\|_F^2 = \sum_{i \in [d_y]} \frac{\sigma^2 s_i^2 (\alpha_i - 1)^2}{(\alpha_i^2 s_i^2 + \sigma^2)^2} = \sum_{i \in [d_y]} \zeta_i (\alpha_i - 1)^2 s_i^2 \sigma^2. \quad (33)$$

Substituting Equations (30) and (33) into Equation (25), we can get the expression for \mathbb{D}_p in Theorem 3.2. \square

A.2. Mixing Time

Assumption A.1. The exact posterior $\pi(x|y)$ is strongly log-concave, i.e., $-\log \pi(x|y)$ is m -strongly convex on \mathbb{R}^d .

Assumption A.2. Log-weight functions are locally Lipschitz. For any $R > 0$, there exist constants $C_a(R) \geq 0$ such that for all $(x, x') \in \text{Ball}(x^*, R)$, $\|w_a(x) - w_a(x')\| \leq C_a(R)\|x - x'\|$.

For the functions $w_l(x)$ and $w_p(x)$, we assume that this condition holds with constants $C_l(R)$ and $C_p(R)$, respectively.

Theorem A.3 (Adapted from Theorem 4.3 in (Chen & Biros, 2026)). *Let $\epsilon \in (0, 1)$. Assume that $\pi_a(x|y)$, $\pi_l(x|y)$ and $\pi_p(x|y)$ are all γ -warm starts with respect to the exact posterior $\pi(x|y)$ (i.e., for any Borel set \mathcal{E} , $\mu_0(\mathcal{E}) \leq \gamma\pi(\mathcal{E})$). Assume that Assumption A.1 and Assumption A.2 hold. For Assumption A.2, suppose that the Lipschitz conditions hold with $C_a(R_a)$, $C_l(R_l)$ and $C_p(R_p) \leq \log 2\sqrt{m}/32$, where*

$$R_a = \max \left\{ \sqrt{\frac{d}{m}} r \left(\frac{\epsilon}{17\gamma} \right), \sqrt{\frac{d}{m}} r \left(\frac{\epsilon}{272\gamma} \right) + \|x^* - x_a^*\| \right\}. \quad (34)$$

$$R_l = \max \left\{ \sqrt{\frac{d}{m}} r \left(\frac{\epsilon}{17\gamma} \right), \sqrt{\frac{d}{m}} r \left(\frac{\epsilon}{272\gamma} \right) \frac{1}{\sigma_{\min}(\tilde{\mathbf{F}}^{-1}\mathbf{F})} + \|x^* - x_l^*\| \right\}, \quad (35)$$

$$R_p = \max \left\{ \sqrt{\frac{d}{m}} r \left(\frac{\epsilon}{17\gamma} \right), \sqrt{\frac{d}{m}} r \left(\frac{\epsilon}{272\gamma} \right) \sigma_{\max}(\mathbf{K}) + \|x^* - x_p^*\| \right\}, \quad (36)$$

where $\sigma_{\min}(\cdot)$ and $\sigma_{\max}(\cdot)$ are the smallest and largest singular values of the matrix, $r(\cdot)$ is a constant defined by

$$r(s) = 2 + 2 \max \left\{ \frac{-\log^{1/4}(s)}{d^{1/4}}, \frac{-\log^{1/2}(s)}{d^{1/2}} \right\}. \quad (37)$$

Then the mixing time for `Approx-IMH` has

$$\tau_{mix}^a(\epsilon) \leq 128 \log \left(\frac{2\gamma}{\epsilon} \right) \max \left(1, \frac{128^2 C_a^2(R_a)}{(\log 2)^2 m} \right). \quad (38)$$

The mixing time for `Latent-IMH` and `Proximal-IMH`, $\tau_{mix}^l(\epsilon)$ and $\tau_{mix}^p(\epsilon)$ satisfy a similar bound with $C_a(R_a)$ replaced by $C_l(R_l)$ and $C_p(R_p)$ respectively.

Proof. The results for `Approx-IMH` and `Latent-IMH` were established in Theorem 4.3 of (Chen & Biros, 2026). We follow a similar argument to the proof of `Approx-IMH` to establish the result for `Proximal-IMH`.

Since

$$\pi_p(x|y) \propto q\left(y - \tilde{\mathbf{A}}\mathbf{K}^{-1}x\right) p(\mathbf{K}^{-1}x),$$

Hence $\pi_p(x|y)$ is $m\sigma_{\min}^2(\mathbf{K}^{-1})$ -strongly log-concave. Consequently, there exists a constant $c_2 > 0$ such that

$$\pi_p(\text{Ball}(x_p^*, R_2)) \geq 1 - c_2 s,$$

where

$$R_2 = \sqrt{\frac{d}{m}} \sigma_{\max}(\mathbf{K}) r(c_2 s). \quad (39)$$

If $C_p(R_p) \leq \frac{\log(2\sqrt{m})}{32}$, where R_p satisfies Equation (36), then the conditions of Equation (96) in (Chen & Biros, 2026) are satisfied. The desired mixing-time bound for `Proximal-IMH` therefore follows. \square

Proof of Theorem 3.3. We prove the result by invoking Theorem A.3. Our goal is to derive local Lipschitz constants $C_a(R_a)$, $C_l(R_l)$, and $C_p(R_p)$ for log-weight functions $w_a(x)$, $w_l(x)$, and $w_p(x)$, respectively. Without loss of generality, we assume that the posterior mode is

$$x^* := \arg \min_x \pi(x | y)$$

is located at the origin, i.e., $x^* = 0$. Throughout, we denote by $B(R)$ the Euclidean ball centered at the origin with radius $R > 0$.

1. **Approx-IMH:** The log-weight function is

$$\begin{aligned} w_a(x) &= \log \frac{\pi(x|y)}{\pi_a(x|y)} = -\frac{1}{2\sigma^2} \left(\|y - \mathbf{A}x\|^2 - \|y - \tilde{\mathbf{A}}x\|^2 \right) \\ &= \frac{1}{2\sigma^2} \left(x^\top \underbrace{(\mathbf{A} + \tilde{\mathbf{A}})^\top \Delta \mathbf{A}}_{=: \mathbf{M}_a} x + 2y^\top \Delta \mathbf{A} x \right). \end{aligned} \quad (40)$$

Define the symmetric version of \mathbf{M}_a by $\mathbf{M}_{a,s} = \frac{1}{2} (\mathbf{M}_a + \mathbf{M}_a^\top)$, then $x^\top \mathbf{M}_a x = x^\top \mathbf{M}_{a,s} x$. Thus for any $x_1, x_2 \in B(R_a)$

$$\begin{aligned} |x_1^\top \mathbf{M}_{a,s} x_1 - x_2^\top \mathbf{M}_{a,s} x_2| &= |(x_1 + x_2)^\top \mathbf{M}_{a,s} (x_1 - x_2)| \leq \|\mathbf{M}_{a,s}\| \|x_1 + x_2\| \|x_1 - x_2\| \\ &\leq 4R_a \|\mathbf{A}\| \|\Delta \mathbf{A}\| \|x_1 - x_2\|. \end{aligned} \quad (41)$$

Besides, we have

$$|2y^\top \Delta \mathbf{A} x_1 - 2y^\top \Delta \mathbf{A} x_2| \leq 2\|\Delta \mathbf{A}^\top y\| \|x_1 - x_2\| \leq 2\|y\| \|\Delta \mathbf{A}\| \|x_1 - x_2\|. \quad (42)$$

Combining Equations (40) to (42), we have

$$|w_a(x_1) - w_a(x_2)| \leq \underbrace{\frac{2R_a \|\mathbf{A}\| + \|y\|}{\sigma^2} \|\Delta \mathbf{A}\|}_{=: C_a(R_a)} \|x_1 - x_2\|. \quad (43)$$

When d is large, by Theorem A.3, $R_a \sim \sqrt{\frac{d}{m}}$, thus

$$\begin{aligned} C_a(R_a) &\sim \sqrt{\frac{d}{m}} \frac{\|\mathbf{A}\|}{\sigma^2} \|\Delta \mathbf{A}\|, \\ \tau_{mix}^a &\sim \frac{d}{m^2} \frac{\|\mathbf{A}\|^2}{\sigma^4} \|\Delta \mathbf{A}\|^2. \end{aligned} \quad (44)$$

2. **Latent-IMH:** Denote f as the negative log prior, i.e. $f(x) = -\log p(x)$, then the log-weight function is

$$w_l(x) = \log \frac{\pi(x|y)}{\pi_l(x|y)} = -(f(x) - f(\mathbf{M}_l x)), \quad \mathbf{M}_l := \tilde{\mathbf{F}}^{-1} \mathbf{F}. \quad (45)$$

Thus we have gradient of the log-weight function

$$\begin{aligned} \nabla w_l(x) &= \nabla f(x) - \mathbf{M}_l^\top \nabla f(\mathbf{M}_l x) \\ &= (\mathbf{I} - \mathbf{M}_l^\top) \nabla f(x) + \mathbf{M}_l^\top (\nabla f(x) - \nabla f(\mathbf{M}_l x)) \end{aligned} \quad (46)$$

By assumption in Theorem 3.3, f is L -smooth, thus

$$\begin{aligned} \|\nabla w_l(x)\| &\leq \|\mathbf{I} - \mathbf{M}_l\| \|\nabla f(x)\| + \|\mathbf{M}_l\| \|\nabla f(x) - \nabla f(\mathbf{M}_l x)\| \\ &\leq \|\mathbf{I} - \mathbf{M}_l\| \|\nabla f(x)\| + \|\mathbf{M}_l\| L \|x - \mathbf{M}_l x\| \\ &\leq \|\mathbf{I} - \mathbf{M}_l\| (\|\nabla f(x)\| + L \|\mathbf{M}_l\| \|x\|) \end{aligned} \quad (47)$$

For any $x_1, x_2 \in B(R_l)$, we have

$$|w_l(x_1) - w_l(x_2)| \leq \sup_{x \in B(R_l)} \|\nabla w_l(x)\| \|x_1 - x_2\|. \quad (48)$$

By Equation (47), we have

$$\sup_{x \in B(R_l)} \|\nabla w_l(x)\| \leq \|\mathbf{I} - \mathbf{M}_l\| \left(\sup_{x \in B(R_l)} \|\nabla f(x)\| + LR_l \|\mathbf{M}_l\| \right), \quad (49)$$

where

$$\sup_{x \in B(R_l)} \|\nabla f(x)\| \leq \|\nabla f(0)\| + L\|x\| \leq \|\nabla f(0)\| + LR_l. \quad (50)$$

Substitute into Equation (48):

$$|w_l(x_1) - w_l(x_2)| \leq \underbrace{\|\mathbf{I} - \mathbf{M}_l\| [(1 + \|\mathbf{M}_l\|) LR_l + \|\nabla f(0)\|]}_{=: C_l(R_l)} \|x_1 - x_2\|. \quad (51)$$

When d is large, by Theorem A.3, $R_l \sim \sqrt{\frac{d}{m}}$, thus

$$\begin{aligned} C_l(R_l) &\sim L \sqrt{\frac{d}{m}} (1 + \|\mathbf{M}_l\|) \|\mathbf{I} - \mathbf{M}_l\|, \\ \tau_{mix}^l &\sim \frac{L^2 d}{m^2} (1 + \|\mathbf{M}_l\|)^2 \|\mathbf{I} - \mathbf{M}_l\|^2. \end{aligned} \quad (52)$$

3. Proximal-IMH: Denote $f(x) = -\log p(x)$, by Equation (5), we have Proximal posterior:

$$\pi_p(x|y) \propto \exp \left(-\frac{1}{2\sigma^2} \|\tilde{\mathbf{A}}\mathbf{K}^{-1}x - y\|^2 - f(\mathbf{K}^{-1}x) \right) \quad (53)$$

the log-weight function is

$$w_p(x) = \log \frac{\pi(x|y)}{\pi_p(x|y)} = -\frac{1}{2\sigma^2} \underbrace{\left(\|\mathbf{A}x - y\|^2 - \|\tilde{\mathbf{A}}\mathbf{K}^{-1}x - y\|^2 \right)}_{=: h(x)} - (f(x) - f(\mathbf{K}^{-1}x)). \quad (54)$$

According to Section 3.1, given \tilde{x} , define $x = \mathbf{K}\tilde{x}$. Then x is the solution to the following optimization:

$$\min_x \|\mathbf{A}x - \tilde{\mathbf{A}}\tilde{x}\|^2 + \beta \|x - \tilde{x}\|^2. \quad (55)$$

Taking gradient of the objective, we can get:

$$\mathbf{A}^\top r = -\beta(x - \tilde{x}), \quad r = \mathbf{A}x - \tilde{\mathbf{A}}\tilde{x}. \quad (56)$$

Thus

$$\begin{aligned} h(x) &= h(\mathbf{K}\tilde{x}) = \|\mathbf{A}\mathbf{K}\tilde{x} - y\|^2 - \|\tilde{\mathbf{A}}\tilde{x} - y\|^2 \\ &= \left(\mathbf{A}\mathbf{K}\tilde{x} + \tilde{\mathbf{A}}\tilde{x} - 2y \right)^\top \left(\mathbf{A}\mathbf{K}\tilde{x} - \tilde{\mathbf{A}}\tilde{x} \right) = \left(\mathbf{A}\mathbf{K}\tilde{x} + \mathbf{A}\tilde{x} + \Delta\mathbf{A}\tilde{x} - 2y \right)^\top \left(\mathbf{A}x - \tilde{\mathbf{A}}\tilde{x} \right) \\ &\stackrel{\text{Equation (56)}}{=} -\beta(x + \tilde{x})^\top (x - \tilde{x}) - 2y^\top r + \tilde{x}^\top (\Delta\mathbf{A})^\top r. \end{aligned} \quad (57)$$

For y , we have y generated by some x_0 by $y = \mathbf{A}x_0 + e$, where e is the noise, we neglect the noise term because we discuss the scaling of the mixing time. Thus by Equation (56)

$$y^\top r = x_0^\top \mathbf{A}^\top r = -\beta x_0^\top (x - \tilde{x}). \quad (58)$$

Let $\mathbf{A}^\dagger = (\mathbf{A}^\top \mathbf{A} + \beta \mathbf{I})^{-1} \mathbf{A}^\top$, we have $\mathbf{K} = \mathbf{I} + \mathbf{A}^\dagger \Delta \mathbf{A}$. For the last term in Equation (57), we have

$$\begin{aligned} \tilde{x}^\top (\Delta \mathbf{A})^\top r &= \tilde{x}^\top (\Delta \mathbf{A})^\top (\mathbf{A} \mathbf{K} \tilde{x} - \tilde{\mathbf{A}} \tilde{x}) = \tilde{x}^\top (\Delta \mathbf{A})^\top (\mathbf{A} (\mathbf{I} + \mathbf{A}^\dagger \Delta \mathbf{A}) - \tilde{\mathbf{A}}) \tilde{x} \\ &= \tilde{x}^\top (\Delta \mathbf{A})^\top (\mathbf{A} \mathbf{A}^\dagger - \mathbf{I}) (\Delta \mathbf{A}) \tilde{x}. \end{aligned} \quad (59)$$

Substituting Equations (58) and (59) into Equation (57), we can get

$$\begin{aligned} h(x) &= -\beta(x + \mathbf{K}^{-1}x)^\top (x - \mathbf{K}^{-1}x) + 2\beta x_0^\top (x - \mathbf{K}^{-1}x) + (\mathbf{K}^{-1}x)^\top (\Delta \mathbf{A})^\top (\mathbf{A} \mathbf{A}^\dagger - \mathbf{I}) (\Delta \mathbf{A}) (\mathbf{K}^{-1}x) \\ &= -\beta x^\top (\mathbf{I} + \mathbf{K}^{-1})^\top (\mathbf{I} - \mathbf{K}^{-1}) x - 2\beta x_0^\top (\mathbf{I} - \mathbf{K}^{-1}) x + x^\top (\mathbf{K}^{-T} (\Delta \mathbf{A})^\top (\mathbf{A} \mathbf{A}^\dagger - \mathbf{I}) (\Delta \mathbf{A}) \mathbf{K}^{-1}) x. \end{aligned} \quad (60)$$

Thus, for any $x_1, x_2 \in B(R_p)$, we have

$$\begin{aligned} \frac{1}{2\sigma^2} |h(x_1) - h(x_2)| &\leq \frac{\beta}{2\sigma^2} \|\mathbf{I} + \mathbf{K}^{-1}\| \|\mathbf{I} - \mathbf{K}^{-1}\| \|x_1 + x_2\| \|x_1 - x_2\| \\ &\quad + \frac{\beta}{\sigma^2} \|\mathbf{I} - \mathbf{K}^{-1}\| \|x_0\| \|x_1 - x_2\| + \frac{\|\mathbf{A} \mathbf{A}^\dagger - \mathbf{I}\|}{\sigma^2} \|\mathbf{K}^{-1}\|^2 \|\Delta \mathbf{A}\|^2 \|x_1 + x_2\| \|x_1 - x_2\| \\ &\lesssim R_p \|\mathbf{I} + \mathbf{K}^{-1}\| \|\mathbf{I} - \mathbf{K}^{-1}\| \|x_1 - x_2\|, \end{aligned} \quad (61)$$

where we derived the last equation by using $\beta = \Theta(\sigma^2)$.

As for the local Lipschitzness of another term in Equation (54), we adopt what we derived for the Latent-IMH, i.e. by (51), we have for any $x_1, x_2 \in B(R_p)$,

$$|(f(x_1) - f(\mathbf{K}^{-1}x_1)) - (f(x_2) - f(\mathbf{K}^{-1}x_2))| \leq \|\mathbf{I} - \mathbf{K}^{-1}\| [(1 + \|\mathbf{K}^{-1}\|)LR_p + \|\nabla f(0)\|] \|x_1 - x_2\|. \quad (62)$$

Combining Equations (54), (61) and (62), we have for any $x_1, x_2 \in B(R_p)$

$$|w_p(x_1) - w_p(x_2)| \lesssim C_p(R_p) \|x_1 - x_2\|, \quad (63)$$

where

$$C_p(R_p) = (L + 1)R_p(1 + \|\mathbf{K}^{-1}\|) \|\mathbf{I} - \mathbf{K}^{-1}\|. \quad (64)$$

When d is large, by Theorem A.3, $R_p \sim \sqrt{\frac{d}{m}}$, and

$$\tau_{mix}^p \sim \frac{d(L + 1)^2}{m^2} (1 + \|\mathbf{K}^{-1}\|)^2 \|\mathbf{I} - \mathbf{K}^{-1}\|^2. \quad (65)$$

□

A.3. Derivation of Equation (20)

Let $\tilde{\mathbf{A}}G(x)$ denote an approximate forward model and assume that $\Delta \mathbf{A} = \delta \mathbf{A}$ for some $\delta \in (0, 1)$. The residual is $r(\tilde{x}) = \mathbf{A}G(\tilde{x}) - \tilde{\mathbf{A}}G(\tilde{x}) = \delta \mathbf{A}G(\tilde{x})$. Then the Gauss–Newton update from Equation (17) becomes

$$GN(\tilde{x}) := \tilde{x} - \delta (\mathbf{J}(\tilde{x})^\top \mathbf{J}(\tilde{x}) + \beta \mathbf{I})^{-1} \mathbf{J}(\tilde{x})^\top \mathbf{A}G(\tilde{x}), \quad (66)$$

For small residuals r , we neglect second-order terms in the linearization of the Gauss–Newton update Equation (17). Under this approximation, the Jacobian of a single Gauss–Newton step Equation (66) takes the form

$$\begin{aligned} \mathbf{J}_{GN}(\tilde{x}) &= \mathbf{I} - \delta (\mathbf{J}(\tilde{x})^\top \mathbf{J}(\tilde{x}) + \beta \mathbf{I})^{-1} \mathbf{J}(\tilde{x})^\top (\mathbf{A} \mathbf{J}_G(\tilde{x})) \\ &= \mathbf{I} - \delta (\mathbf{J}(\tilde{x})^\top \mathbf{J}(\tilde{x}) + \beta \mathbf{I})^{-1} \mathbf{J}(\tilde{x})^\top \mathbf{J}(\tilde{x}) \\ &= (1 - \delta) \mathbf{I} + \delta \beta (\mathbf{J}^\top(\tilde{x}) \mathbf{J}(\tilde{x}) + \beta \mathbf{I})^{-1}, \end{aligned} \quad (67)$$

where the second equality is derived by the fact that $\mathbf{J}(\tilde{x}) = \mathbf{A}\mathbf{J}_G(\tilde{x})$.

For two arbitrary points \tilde{x}_1 and \tilde{x}_2 , let $\{\lambda_{1,i}\}_{i \in [d_x]}$ and $\{\lambda_{2,i}\}_{i \in [d_x]}$ denote the eigenvalues (in descending order) of $\mathbf{J}^\top(\tilde{x}_1)\mathbf{J}(\tilde{x}_1)$ and $\mathbf{J}^\top(\tilde{x}_2)\mathbf{J}(\tilde{x}_2)$, respectively. The logarithm of the Jacobian determinant ratio can then be expressed as

$$\log \frac{|\det \mathbf{J}_{GN}(\tilde{x}_1)|}{|\det \mathbf{J}_{GN}(\tilde{x}_2)|} = \sum_{i \in [d_x]} \log \frac{1 - \delta \lambda_{1,i}/(\lambda_{1,i} + \beta)}{1 - \delta \lambda_{2,i}/(\lambda_{2,i} + \beta)}. \quad (68)$$

B. Helmholtz Forward Model

B.1. Linearized Helmholtz (Born Approximation) Model

Consider the Helmholtz equation

$$\mathcal{L}(x)u := (-\Delta - k^2 x)u = f, \quad (69)$$

where x denotes the spatially varying contrast parameter and $k > 0$ is the wavenumber. Let x_0 be a known background medium and write

$$x = x_0 + \delta x,$$

where δx is a small perturbation.

Let u_0 denote the background wavefield solving

$$\mathcal{L}(x_0)u_0 = f. \quad (70)$$

Substituting this decomposition into the Helmholtz equation and retaining only first-order terms in δx yields the linearized equation

$$\mathcal{L}(x_0)\delta u = k^2 \delta x u_0, \quad (71)$$

where $\delta u := u - u_0$ denotes the scattered field.

The scattered field can therefore be expressed as

$$\delta u = \mathcal{L}(x_0)^{-1}(k^2 \delta x u_0). \quad (72)$$

This relation defines a linear map from the contrast perturbation δx to the scattered field δu . For convenience, we introduce the operator

$$F := \mathcal{L}(x_0)^{-1}(k^2 \text{diag}(u_0)), \quad (73)$$

so that $\delta u = F \delta x$.

B.2. Nonlinear Forward Model and Adjoint

For the full nonlinear problem, the forward model is given by

$$\begin{cases} \mathcal{L}(x)u = f, & \text{where } \mathcal{L}(x) := -\Delta - k^2 x \\ y = \mathbf{O}u, \end{cases} \quad (74)$$

where the wavefield $u = u(x)$ depends nonlinearly on the contrast parameter x .

Given a current parameter x , the forward wavefield u is computed by solving the Helmholtz equation using GMRES in a matrix-free fashion, without explicitly forming the system matrix.

Adjoint formulation. Let $r := \mathbf{O}u - y$ denote the data residual. The adjoint field v is defined as the solution of the adjoint Helmholtz equation

$$\mathcal{L}(x)^\top v = \mathbf{O}^\top r, \quad (75)$$

Table 1. Distributions of Exact, Approx, Latent and Proximal posteriors for Gaussian prior $p(x) = \mathcal{N}(\mathbf{0}, \mathbf{I})$ and noise $q(e) = \mathcal{N}(\mathbf{0}, \sigma^2 \mathbf{I})$. For Proximal posterior, $\mathbf{K} = (\mathbf{A}^\top \mathbf{A} + \beta \mathbf{I})^{-1} (\mathbf{A}^\top \tilde{\mathbf{A}} + \beta \mathbf{I})$.

Posterior	Distribution	Mean	Covariance	Pseudo-inverse
Exact	$\pi(x y) = \mathcal{N}(\mu, \Sigma)$	$\mu = \mathbf{A}^\dagger y$	$\Sigma = \mathbf{I} - \mathbf{A}^\dagger \mathbf{A}$	$\mathbf{A}^\dagger = \mathbf{A}^\top (\mathbf{A} \mathbf{A}^\top + \sigma^2 \mathbf{I})^{-1}$
Approx	$\pi_a(x y) = \mathcal{N}(\mu_a, \Sigma_a)$	$\mu_a = \mathbf{A}_a^\dagger y$	$\Sigma_a = \mathbf{I} - \mathbf{A}_a^\dagger \tilde{\mathbf{A}}$	$\mathbf{A}_a^\dagger = \tilde{\mathbf{A}}^\top (\tilde{\mathbf{A}} \tilde{\mathbf{A}}^\top + \sigma^2 \mathbf{I})^{-1}$
Latent	$\pi_l(x y) = \mathcal{N}(\mu_l, \Sigma_l)$	$\mu_l = \mathbf{A}_l^\dagger y$	$\Sigma_l = \mathbf{F}^{-1} \tilde{\mathbf{F}} \tilde{\Sigma}_a \tilde{\mathbf{F}}^\top \mathbf{F}^{-\top}$	$\mathbf{A}_l^\dagger = \mathbf{F}^{-1} \tilde{\mathbf{F}} \mathbf{A}_a^\dagger$
Proximal	$\pi_p(x y) = \mathcal{N}(\mu_p, \Sigma_p)$	$\mu_p = \mathbf{A}_p^\dagger y$	$\Sigma_p = \mathbf{K} \Sigma_a \mathbf{K}^\top$	$\mathbf{A}_p^\dagger = \mathbf{K} \mathbf{A}_a^\dagger$

Effects	\log_{10} SNR	$\frac{\ \mathbf{F} - \tilde{\mathbf{F}}\ }{\ \mathbf{F}\ }$	d_y/d	d
Noise level	0.5—4.0	6%	0.2	500
Operator error	2.5	2%—21%	0.2	500
Observation ratio	2.5	6%	0.05—0.5	500
Dimension	2.5	6%	0.2	100—2000

Table 2. Experimental setup for comparing \mathbb{D}_a , \mathbb{D}_l and \mathbb{D}_p .

with adjoint boundary conditions consistent with the forward problem.

The gradient of the data misfit functional

$$\Phi(x) := \frac{1}{2} \|\mathbf{O}u - y\|^2 \quad (76)$$

with respect to x is given by

$$\nabla_x \Phi(x) = -k^2 u \odot v, \quad (77)$$

where \odot is the pointwise (Hadamard) product.

C. Additional Experimental Details

C.1. Proposal comparisons in Section 3.2

In Table 1, we provide the Gaussian formulation of different posteriors when prior is normal and noise is Gaussian distribution with variance σ^2 . Table 2 presents the experimental setup for the sensitivity test on KL divergence in Figure 1.

C.2. Bimodal test in Section 4.1

The histogram of the projection of prior samples in the bimodal test (see Equation (21)) is plotted in Figure 9.

C.3. MNIST inverse problem in Section 4.2

A and $\tilde{\mathbf{A}}$ construction in Tests VI and VII (Section 4.2). We consider the linearized Helmholtz forward model introduced in Section B.1. In our experiments, the parameter x is represented on a 28×28 grid corresponding to MNIST images, while the wavefield u is discretized on a finer 100×100 spatial grid. Consequently, the dimensions of the parameter and wavefield are $d_x = 784$ and $d_u = 10^4$, respectively. The wave number is set to $k = 2.4\pi$ in our experiments.

The linearized operator F defined in Equation (73) is discretized on a two-dimensional uniform grid using a second-order finite-difference scheme with homogeneous Neumann boundary conditions; we denote the fine-grid inverse Helmholtz operator by $\mathbf{F} \in \mathbb{R}^{d_u \times d_u}$. A sparse prolongation operator $\mathbf{P} \in \mathbb{R}^{d_u \times d_x}$ maps the parameter x from the coarse 28×28 grid to the fine 100×100 grid on which the Helmholtz equation is solved. With an observation operator $\mathbf{O} \in \mathbb{R}^{d_y \times d_u}$, the resulting fine-scale forward operator $\mathbf{A} \in \mathbb{R}^{d_y \times d_x}$ is defined as

$$\mathbf{A} := \mathbf{O} \mathbf{F} \mathbf{P}. \quad (78)$$

The corresponding forward model from the latent variable z to the observation y is then given by

$$y = \mathbf{A} G(z) + e, \quad (79)$$

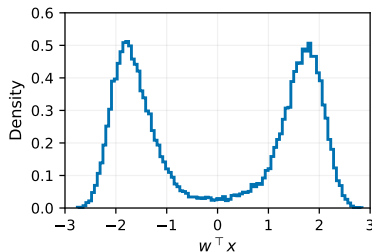


Figure 9. Histogram of the projection of prior samples in the bimodal test (see Equation (21)).

Table 3. Dimensions of parameters in Tests VI and VII in Section 4.2.

d_z	d_x	d_u	\tilde{d}_u	d_y
128	784 (= 28 ²)	10 ⁴ (= 100 ²)	{35 ² , 20 ² }	100

where $G : \mathbb{R}^{d_z} \rightarrow \mathbb{R}^{d_x}$ denotes the decoder of the variational autoencoder (VAE).

To construct the approximate operator $\tilde{\mathbf{A}}$, we introduce coarser spatial grids of size $\tilde{n}_u \times \tilde{n}_u$ for the wavefield u , where $\tilde{n}_u \in \{20, 35\}$ in our experiments. We denote the corresponding discretized Helmholtz operator on the coarse grid by $\tilde{\mathbf{F}} \in \mathbb{R}^{\tilde{d}_u \times \tilde{d}_u}$, with $\tilde{d}_u = \tilde{n}_u^2$. Sparse prolongation operators $\mathbf{P}_u \in \mathbb{R}^{d_u \times \tilde{d}_u}$ and $\mathbf{P}_x \in \mathbb{R}^{\tilde{d}_u \times d_x}$ are used to map vectors between the coarse and fine grids. The resulting approximate forward operator is then defined as

$$\tilde{\mathbf{A}} := \mathbf{O} \mathbf{P}_u \tilde{\mathbf{F}} \mathbf{P}_x. \quad (80)$$

The dimensions involved in the construction of \mathbf{A} and $\tilde{\mathbf{A}}$ are summarized in Table 3, and schematic diagrams of the corresponding matrix factorizations are shown in Figure 10.

Jacobian Determinant Diagnostics of the Gauss–Newton Correction. Figure 11 examines the variability of the Jacobian determinant associated with a single Gauss–Newton correction across posterior samples and operator approximation levels. In the left panels, we plot the sorted log determinants of the Gauss–Newton Jacobian evaluated at 2000 randomly selected posterior samples. As the relative operator approximation error $\|\mathbf{A} - \tilde{\mathbf{A}}\|/\|\mathbf{A}\|$ increases, the log-determinant values exhibit a systematic shift and increased spread, indicating stronger local volume distortion induced by the correction map. The right plots assess relative variability by considering ratios of Jacobian determinants between 2000 randomly selected pairs of approximate posterior samples from $\pi_a(x | y)$. Across all tests, these ratios remain tightly concentrated around one, with the 5%–95% quantile range remaining narrow even at larger approximation errors. This suggests that, despite changes in absolute scale, the Gauss–Newton transformation induces relatively uniform local volume changes across the posterior in the test.

C.4. Nonlinear Helmholtz test in Section 4.3

Forward operator $\mathbf{A}_i(x)$ and its approximation $\tilde{\mathbf{A}}_i(x)$. The nonlinear forward model and its adjoint are introduced in Section B.2. The nonlinear Helmholtz operator is defined as

$$\mathcal{L}(x) := -\Delta - k^2 x.$$

The medium parameter x is represented on a 32×32 uniform grid over the domain $[0, 1] \times [0, 1]$. The Helmholtz operator $\mathcal{L}(\cdot)$ is discretized on a finer 128×128 uniform grid using a second-order finite-difference scheme with homogeneous Neumann boundary conditions; we denote the resulting nonlinear discretized operator by $\mathbf{L}(\cdot)$. The wavenumber is set to $k = 3.4\pi$ in this test.

We consider $n_s = 4$ distinct source terms $\{f_i\}_{i \in [n_s]}$. For each source, the corresponding observation is generated by

$$y_i = \mathbf{O} \mathbf{L}^{-1}(\mathbf{P}x) f_i + e_i, \quad i \in [n_s], \quad (81)$$

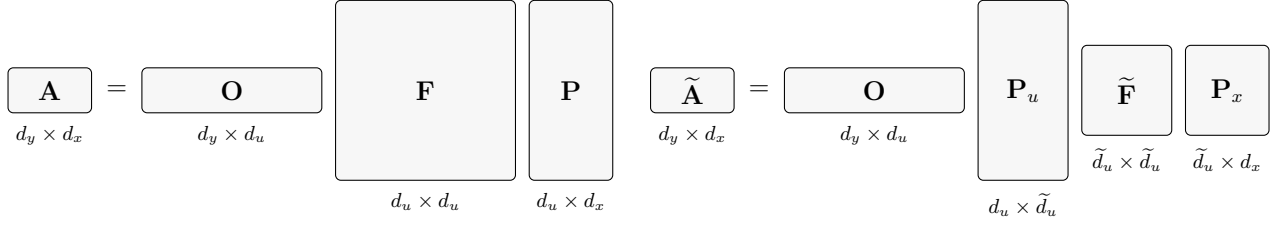


Figure 10. Matrix constructions of \mathbf{A} and $\tilde{\mathbf{A}}$ in Tests VI and VII in Section 4.2. Left: $\mathbf{A} = \mathbf{O} \mathbf{F} \mathbf{P}$. Right: $\tilde{\mathbf{A}} = \mathbf{O} \mathbf{P}_u \tilde{\mathbf{F}} \mathbf{P}_x$. In our setting $d_y < d_x < d_u$, and $\tilde{d}_u < d_u$.

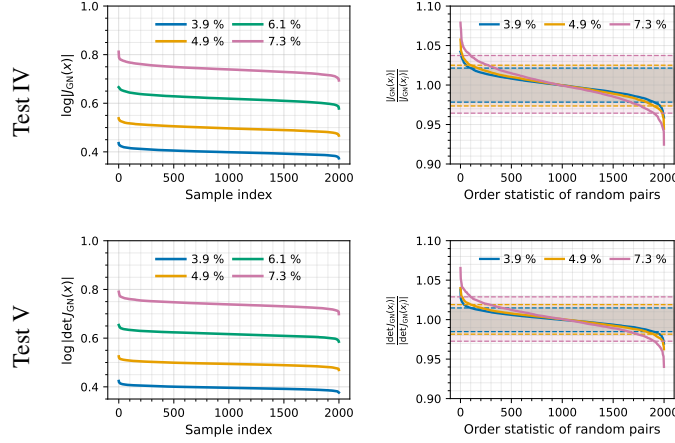


Figure 11. Jacobian log-determinant diagnostics for the Gauss–Newton correction. Each row corresponds to one test case. **Left:** Sorted values of the log determinant of the Jacobian of a single Gauss–Newton transformation, evaluated at 2000 randomly selected posterior samples from $\pi_a(x | y)$. **Right:** Order statistics of ratios of Jacobian determinants between 2000 randomly selected pairs of posterior samples from $\pi_a(x | y)$, i.e., $\det J_{\text{GN}}(x_i) / \det J_{\text{GN}}(x_j)$. The numbers shown in the legends indicate the relative operator approximation error $\|\mathbf{A} - \tilde{\mathbf{A}}\| / \|\mathbf{A}\|$. In the right panels, dashed lines denote the 5%–95% quantile range.

where \mathbf{P} denotes a prolongation operator mapping the medium parameter from the coarse grid to the fine grid, and \mathbf{O} is the observation operator. Accordingly, the nonlinear forward operator is defined as

$$\mathbf{A}_i(x) := \mathbf{O} \mathbf{L}^{-1}(\mathbf{P}x) f_i, \quad i \in [n_s]. \quad (82)$$

To construct an approximate forward model, we introduce a coarser 64×64 grid for the wavefield discretization. Let $\tilde{\mathbf{L}}(\cdot)$ denote the discretized nonlinear Helmholtz operator on this coarse grid. Analogous to the linear construction in Equation (80), we define the approximate nonlinear forward operator as

$$\tilde{\mathbf{A}}_i(x) := \mathbf{O} \mathbf{P}_u \tilde{\mathbf{L}}^{-1}(\mathbf{P}_x x) f_i, \quad i \in [n_s], \quad (83)$$

where \mathbf{P}_x and \mathbf{P}_u are sparse prolongation operators used to map the medium parameter and wavefield, respectively, from coarse grids to the fine grid. Table 4 summarizes the dimensions of parameters involved in this test.

GMRES solver with Neumann–DCT preconditioning. We solve the (nonlinear) Helmholtz linear systems arising in Equation (82) and Equation (83) and related adjoint computations using GMRES with a matrix-free spectral preconditioner. The preconditioner is based on a constant-coefficient approximation of the Helmholtz operator,

$$\mathcal{M} := -\Delta + k^2(1 + \bar{x}),$$

where \bar{x} denotes the spatial average of the medium parameter x and homogeneous Neumann boundary conditions are imposed. On a uniform $n \times n$ grid, the Neumann Laplacian is diagonalized by the two-dimensional discrete cosine transform (DCT). Let Λ denote the eigenvalues of $-\Delta$ under Neumann boundary conditions. Applying \mathcal{M}^{-1} to a vector v is implemented by reshaping v to an $n \times n$ array, computing its 2D DCT, dividing entrywise by $\Lambda + k^2(1 + \bar{x})$, and transforming back via the inverse 2D DCT. This results in an efficient $\mathcal{O}(n^2 \log n)$ preconditioner application that substantially accelerates GMRES convergence.

Table 4. Dimensions of parameters in the nonlinear Helmholtz test in Section 4.3.

d_x	d_u	\tilde{d}_u	d_y
1024 (= 32^2)	16,384 (= 128^2)	4,096 (= 64^2)	512

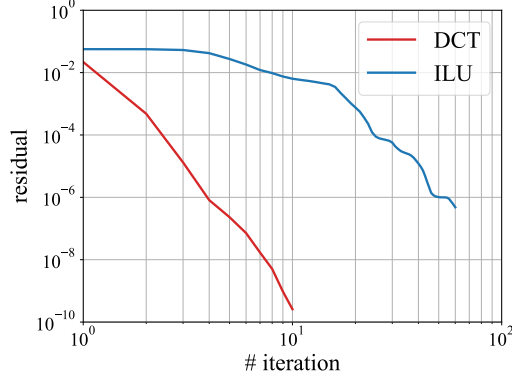


Figure 12. Effect of preconditioning on GMRES convergence for the nonlinear Helmholtz test.

Proposal for Proximal-IMH. The objective of the proximal correction in this multiple-source setting is the following: let $\tilde{x} \sim \pi_a$, the proposal of Proximal-IMH is

$$x \leftarrow \arg \min_x \sum_{i \in [n_s]} \left\| \mathbf{A}_i(x) - \tilde{\mathbf{A}}_i(\tilde{x}) \right\|^2 + \beta \|x - \tilde{x}\|^2. \quad (84)$$

One Gauss–Newton step formulation for Equation (84). A single Gauss–Newton step to optimize Equation (84) initialized at \tilde{x} is given by

$$\begin{cases} x \leftarrow \tilde{x} + \delta x, \\ \left(\sum_{i=1}^{n_s} \mathbf{J}_i(\tilde{x})^\top \mathbf{J}_i(\tilde{x}) + \beta \mathbf{I} \right) \delta x = - \sum_{i=1}^{n_s} \mathbf{J}_i(\tilde{x})^\top \left(\mathbf{A}_i(\tilde{x}) - \tilde{\mathbf{A}}_i(\tilde{x}) \right), \end{cases} \quad (85)$$

where $\mathbf{J}_i(\tilde{x}) := \left. \frac{\partial \mathbf{A}_i(x)}{\partial x} \right|_{x=\tilde{x}}$ denotes the Jacobian of \mathbf{A}_i evaluated at \tilde{x} .

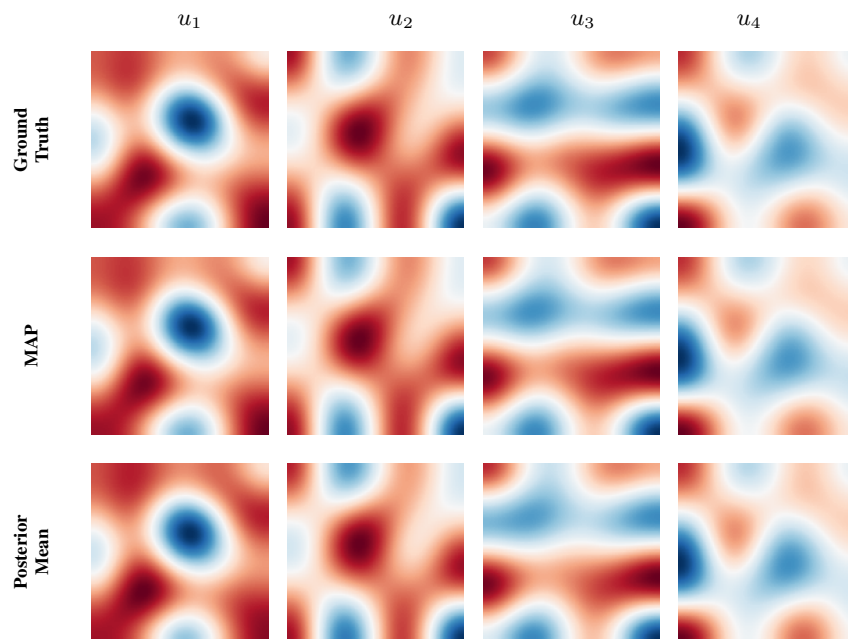


Figure 13. Wavefields $\{u_i = \mathcal{L}(x)^{-1} f_i\}_{i=1}^4$ for the nonlinear Helmholtz test. Each column corresponds to a distinct source f_i . **Top:** Ground-truth wavefields. **Middle:** Wavefields obtained from the MAP estimate. **Bottom:** Posterior mean wavefields computed from posterior samples.